Research Square

Preprints are preliminary reports that have not undergone peer review.
They should not be considered conclusive, used to inform clinical practice,
or referenced by the media as validated information.

Hydrography-constrained AMOC reconstruction shows freshwater-driven decline and fading thermal compensation

Sang-Ki Lee

Sang-Ki.Lee@noaa.gov

NOAA AOML https://orcid.org/0000-0002-4047-3545

Fabian Gomez

Northern Gulf Institute, Mississippi State/NOAA https://orcid.org/0000-0002-2335-478X

Dongmin Kim

CIMAS/University of Miami https://orcid.org/0000-0002-1465-2945

Hosmay Lopez

NOAA/Atlantic Oceanographic and Meteorological Laboratory https://orcid.org/0000-0002-8422-8699

Shenfu Dong

NOAA/AOML https://orcid.org/0000-0001-8247-8072

Rick Lumpkin

Article

Keywords:

Posted Date: July 13th, 2026

DOI: https://doi.org/10.21203/rs.3.rs-10195170/v1

License: This work is licensed under a Creative Commons Attribution 4.0 International License.
Read Full License

Additional Declarations: There is **NO** Competing Interest.

Hydrography-constrained AMOC reconstruction shows freshwater-driven decline and fading thermal compensation

Sang-Ki Lee[1], Fabian A. Gomez[2,1], Dongmin Kim[3,1], Hosmay Lopez[1], Shenfu Dong[1], & Rick Lumpkin[1*]

[1]NOAA Atlantic Oceanographic and Meteorological Laboratory, Miami, FL, USA

[2]Northern Gulf Institute, Mississippi State University, Mississippi State, MS, USA

[3]Cooperative Institute for Marine and Atmospheric Studies, University of Miami, Miami, FL, USA

[*]Retired

July 2026

Corresponding author: Dr. Sang-Ki Lee (Sang-Ki.Lee@noaa.gov), NOAA, Atlantic Oceanographic and Meteorological Laboratory, 4301 Rickenbacker Causeway, Miami, FL 33149, USA.

Abstract

The historical evolution of the Atlantic Meridional Overturning Circulation (AMOC) remains debated due to limited continuous observations. To bridge this gap, we leverage historical hydrographic data spanning 1955 to 2022 to constrain a high-resolution global ocean model. Here, we show an overall weakening of the AMOC relative to a 1955–1964 baseline, interrupted by a transient recovery during 1995–2004. The regional footprint of this weakening shifts over time. While earlier reductions (~7% during 1965–1994) are driven by suppressed dense water formation in the subpolar North Atlantic, steeper recent declines (~11% during 2005–2022) stem from combined reductions across the subpolar North Atlantic and Nordic Seas, despite partially compensating increases in the Arctic Ocean. Sensitivity experiments reveal that the AMOC weakening is overwhelmingly driven by a long-term freshening regime, manifested by repeated episodes of high-latitude salinity anomalies—occurring during the 1970s–1990s and again in recent years—that are broadly tied to Arctic export and Greenland ice melt. Finally, while a relatively cold thermal state during 1975–2004 partially buffers the freshwater-driven decline, this thermal compensation is absent during 2005–2022 due to anomalous warming of the Nordic Seas and the Labrador Current, acting alongside the freshwater forcing to drive the steeper modern decline of the AMOC.

Introduction

A broad consensus exists among Coupled Model Intercomparison Project (CMIP) models that the Atlantic Meridional Overturning Circulation (AMOC) will significantly weaken by the end of the 21st century under increasing anthropogenic greenhouse gas forcing[1-5]. A large-scale slowdown of the AMOC would disrupt the interhemispheric redistribution of oceanic heat, salt, nutrients, and carbon, with far-reaching implications for marine ecosystems, coastal sea levels, climate, and extreme weather patterns[6-12]. Reliably predicting the AMOC's future trajectory requires an in-depth understanding of its historical evolution. However, continuous direct observational records from dedicated monitoring arrays, such as RAPID, OSNAP, and SAMBA, only commenced within the last two decades[13-15]; thus, capturing AMOC's long-term historical evolution remains a significant challenge.

To bridge this gap, proxy records (e.g., sea surface temperature-based) and surface-forced prognostic numerical models have been widely used[16-20]. However, proxy records are inherently indirect, and prognostic models often face challenges in fully resolving or representing key localized processes, such as Greenland-Scotland Ridge overflows and ice-sheet melting[21,22]. Additionally, the standard practice of restoring surface salinity to long-term climatologies to prevent model drift can artificially suppress critical freshwater feedbacks and distort simulated AMOC variability. As such, the historical evolution of the AMOC and its driving mechanisms remain heavily debated[23-31].

Further complicating this debate, the AMOC is not driven by a single, localized point of deep-water formation[32]. Instead, its strength is intrinsically tied to a shifting balance of dense water formation via open-ocean convection and diapycnal mixing along current pathways across multiple regions, including the subpolar North Atlantic (Labrador Sea, Irminger Sea, and Iceland

Basin), the Nordic Seas (Iceland Sea, Norwegian Sea, and Greenland Sea), and the Arctic Ocean[32-42]. In particular, recent studies suggest that the relative contributions of these distinct basins are evolving, emphasizing the increasingly critical roles played by the Nordic Seas and the Arctic Ocean[37,40-42]. Yet, precisely mapping how the regional footprint of dense water formation has shifted in the past decades remains difficult without a unified, observation-based framework.

Furthermore, identifying the precise physical drivers of these interdecadal shifts requires untangling the competing influences of salinity and temperature. While increasing freshwater fluxes from Arctic export and Greenland ice melt[43-51], coupled with a reduction in wintertime brine rejection from retreating local sea ice[52,53] have likely suppressed deep convection by enhancing upper-ocean stratification, historical cooling in the subpolar North Atlantic—manifesting as the warming hole[16,17,54-58]—should provide stabilizing negative feedback, partially offsetting this high-latitude buoyancy gain. However, the long-term stability of this critical temperature feedback—especially in the face of recent Arctic warming and potential southward advection of the excess heat—remains largely unexplored. If this historical thermal buffer is eroding or reversing, the destabilizing impact of continued freshwater forcing on the AMOC may be substantially amplified in the future.

The limitations inherent in current observations, proxy records, and prognostic models highlight a critical need to leverage historical hydrographic data to reliably quantify the AMOC's past trajectory, map its evolving spatial structure, and isolate its driving mechanisms. Building on recent successes in reproducing directly observed AMOC transport values across multiple transects[37,59], here we use a hydrography-based robust diagnostic framework to estimate the interdecadal changes of the AMOC since the mid-1950s and trace its spatial footprint across the

subpolar North Atlantic, Nordic Seas, and Arctic Ocean. Specifically, we conduct a series of global ocean and sea-ice model simulations, restoring temperature and salinity fields toward historical observations for each decade between 1955 and 2022 (see Methods). Through this approach, we identify an overall weakening of the AMOC superimposed on prominent decadal variability, marked by a distinct northward expansion of the decline into the Nordic Seas. Furthermore, by decoupling the competing influences of salinity and temperature anomalies, we demonstrate that the decline is primarily freshwater-driven and identify a recent erosion of the system's historical thermal buffer.

Results

The 1955–1964 baseline state. Before quantifying the historical evolution of the AMOC and its regional components, we first establish its mean state during the 1955–1964 baseline period, the first decade of systematic global hydrographic sampling[60]. By calculating the AMOC streamfunction in potential density space (ρ_2), our hydrography-based robust diagnostic framework captures distinct water mass transformations across the subpolar North Atlantic (45°N–70°N, MOC_{SPO}), the northern Nordic Seas and Baffin Bay (70°N–80°N, hereafter simply the northern Nordic Seas; MOC_{NOR}), and the Arctic Ocean (80°N–90°N, MOC_{ARC}; Fig. 1; see Methods). During this baseline period, the AMOC exhibits a robust, large-scale overturning structure. At the 45°N transect, which integrates the dense water formation poleward of this latitude, the maximum overturning streamfunction reaches 20.75 *Sv* at a potential density (ρ_2) of approximately 1036.6 $kg\ m^{-3}$ (Fig. 1b). This total overturning transport can be partitioned into its distinct regional components.

The open-ocean convection and diapycnal mixing occurring within the subpolar North

Atlantic (MOC_{SPO}, Fig. 1b) account for the largest fraction of this transport (11.92 *Sv*), which compares favorably with previously estimated subpolar deep water mass formation rates (e.g., ~9 *Sv*; and up to ~12.5 *Sv*)[61,62]. Further north, the system captures a transport of 8.83 *Sv* crossing the 70°N transect (Fig. 1c), which is in reasonable agreement with the ~8.0 *Sv* observational estimate of total Atlantic Water outflow crossing the Greenland-Scotland Ridge[63] and other observational estimates of overturning across the ridge (e.g., ~7.9 *Sv*; ~7.7 *Sv*)[64,65]. This northern transport is further partitioned into a 4.31 *Sv* contribution from dense water formation within the northern Nordic Seas (MOC_{NOR}) and a prominent 4.53 *Sv* overturning cell across the Fram Strait and Barents Sea at 80°N, representing dense water formation within the Arctic Ocean (MOC_{ARC}, Fig. 1d). This 4.53 *Sv* overturning transport is largely consistent with the long-term mooring-based estimates of the combined Atlantic Water import to the Arctic Ocean across the Fram Strait (~3.0 *Sv*)[66] and the Barents Sea Opening (~2.0 *Sv*)[67]. Together, these regional contributions of dense water formation balance the poleward transport of 20.75 *Sv* in the AMOC's upper limb ($\rho_2 \lesssim$ 1036.6 *kg* m^{-3}) during the 1955–1964 baseline, serving as the reference point for evaluating the subsequent interdecadal evolution and the shifting spatial footprint of dense water formation.

Sustained decline (1965–1994) and partial recovery (1995–2004). Following the 1955–1964 baseline period, our robust diagnostic framework identifies a prolonged period of modest AMOC weakening spanning the next three decades (~7% reduction at 45°N during 1965–1994; Figs. 2b-d, S1d-f). Relative to the baseline, the total overturning transport at 45°N exhibits consistent interdecadal reductions, dropping by 1.49 *Sv* during 1965–1974 (Figs. 2h, S1l) and reaching a peak decline of 1.53 *Sv* during 1985–1994 (Figs. 2f, S1j)—decades that closely coincide with the well-documented Great Salinity Anomalies[44,68-71].

By decomposing these reductions into their regional components, it becomes evident that this sustained weakening is overwhelmingly driven by suppressed dense water formation within the subpolar North Atlantic (Figs. 2f-h, S1j-l). Across all three decades between 1965 and 1994, this subpolar sinking (MOC_{SPO}) exhibits deficits relative to the baseline period (e.g., drops of 1.58 *Sv* in 1965–1974 and 1.54 *Sv* in 1985–1994), broadly matching the total AMOC decline at 45°N. While dense water formation in the northern Nordic Seas initially shows a compensatory increase (+0.54 *Sv* in 1965–1974; Figs. 2h, S1l), this northern buffer fades in subsequent decades, allowing the subpolar deficits to dominate the broader AMOC slowdown. Notably, the deep portion of the AMOC's lower limb ($\rho_2 \gtrsim 1037\ kg\ m^{-3}$) weakens during these subsequent decades (Fig. 2b, c, S1d, e), indicating that even without a sharp drop in total transport amplitude, the southward return flow from the northern Nordic Seas becomes less dense during 1975–1994 (Fig. S2c, g).

The prolonged AMOC decline spanning 1965–1994 is interrupted by a distinct, partial recovery over the 1995–2004 decade (Fig. 2a). During this interval, the total AMOC deficit at 45°N diminishes to just 0.76 *Sv* relative to the baseline (Fig. 2e). Our regional breakdown reveals that this recovery is driven by a combination of an easing subpolar deficit and a shift in the spatial footprint of dense water formation further north. Specifically, although subpolar dense water formation remains suppressed relative to the baseline (by 0.97 *Sv*), this deficit is markedly attenuated compared to the 1.54 *Sv* deficit of the preceding decade. This easing of the subpolar deficit reflects a lagged oceanic adjustment to the well-documented deepest and densest Labrador Sea Water (LSW) formed in the early to mid-1990s, which was driven by a strong positive phase of the North Atlantic Oscillation (NAO)[72-76]. In tandem with this subpolar recovery, the 1995–2004 partial rebound is further facilitated by a notable strengthening of dense

water formation within the Arctic Ocean (+0.47 *Sv*). Together, these regional dynamics partially offset the sustained deficits of the previous decades (1965–1994), temporarily stabilizing the broader AMOC system.

Resumed and steepened decline (2005–2022). The temporary stabilization captured during the 1995–2004 decade ends after the turn of the century, marking the steepest period of AMOC decline in the historical record (~11% reduction at 45°N during 2005–2022; Fig. 3). During 2005–2014, the total overturning transport at 45°N weakens by 2.34 *Sv* relative to the baseline (Fig. 3f). Decomposing this transport reveals that the renewed slowdown is primarily driven by a decline in dense water formation within the subpolar North Atlantic, where the anomaly reaches -2.63 *Sv*. This drop far exceeds the opposing, yet insufficient, buffering effect of the Arctic Ocean (+0.80 *Sv*; Fig. 3h). Notably, during this same decade, the northern Nordic Seas also exhibit a 0.51 *Sv* deficit, signaling the initial weakening of this northern buffer. Nevertheless, because the concurrent increase in dense water formation in the Arctic Ocean acts as a counterweight, the net transport of dense water across 70°N exhibits continued stability (+0.29 *Sv*; Fig. 3g). This regional buffering effect is broadly in line with the high-latitude overturning stability reported in a recent study[41].

In the most recent period (2015–2022), while the total AMOC transport at 45°N remains weakened with a negative anomaly of -2.15 *Sv* (Fig. 3b), our robust diagnostic framework reveals a notable shift in the underlying regional drivers of this continued decline. While the subpolar anomaly eases moderately to -1.45 *Sv*, this localized partial recovery is offset by a reduction further north. In particular, dense water formation within the northern Nordic Seas (MOC_{NOR}) undergoes a substantial decline, falling by 1.12 *Sv*, representing a ~26% reduction

(Fig. 3c). Consequently, the southward transport of dense water across the 70°N transect reaches its most pronounced negative anomaly (-0.70 *Sv*) in the historical record, despite the persistent buffering effect of the Arctic Ocean (+0.42 *Sv*; Fig. 3d).

Ultimately, these recent decades demonstrate that the interdecadal AMOC weakening is no longer confined to the subpolar North Atlantic. While dense water formation in the northern Nordic Seas remains relatively stable throughout much of the 20th century, this regional resilience ends after 1995–2004. Specifically, the upper limb of the AMOC becomes increasingly buoyant, preventing it from undergoing sufficient densification in the subpolar and Nordic regions. This increase in buoyancy is clearly reflected in an overall shift of the upper limb toward lower density classes (Fig. 3). Consequently, these excessively buoyant surface waters are forced to travel further northward, penetrating beyond the Fram Strait and Barents Sea into the Arctic Ocean, where dense water formation finally takes place (Fig. 3d, h)[41]. While an increase in dense water formation within the Arctic Ocean provides a partial buffer, it is insufficient to offset the deficit emerging in the northern Nordic Seas during 2015–2022. This transition marks a critical erosion of the system's historical northern stability, sustaining the AMOC's weakened state through the most recent decade.

Long-term suppression and interdecadal shifts of open-ocean convection. To identify the physical mechanisms underlying the interdecadal transport anomalies, we first examine the changes in open-ocean convection, as represented by late-winter (March) Mixed Layer Depth (MLD) anomalies (Fig. 4). While early hydrographic observations from WOCE and recent observational evidence from OSNAP suggest that open-ocean convection in the Labrador Sea plays a smaller role in the mean state of the AMOC than traditionally assumed[32,77,78], it remains a

208 vital driver of the AMOC's interdecadal variability and long-term changes[75,76]. In agreement
209 with these findings, our results show that the sustained AMOC weakening is strongly coupled
210 with the suppression of open-ocean convection in the Labrador Sea and across other key
211 formation regions of the North Atlantic.

212 During the partial AMOC recovery period of 1995–2004, the Labrador Sea retains a
213 deepened mixed layer (Fig. 4c)—a residual imprint of the deepest and densest LSW formed
214 during the early to mid-1990s, which was driven by a prolonged positive phase of the NAO[70-74].
215 Therefore, this period provides a clear modern baseline, representing the most recent instance of
216 a lagged overturning response following a robust convective state. However, this resilience ends
217 as the system enters the 21st century. During the period of most significant AMOC decline at
218 45°N (2005–2014), the Labrador Sea exhibits a widespread and pronounced reduction in MLD
219 (Fig. 4b). This aligns well with the stark reduction in dense water formation in the subpolar
220 region during this period (ΔMOC_{SPO} ~ -2.63 *Sv*), capturing the well-documented suppression of
221 convection in observational records[79].

222 In the most recent decade (2015–2022), the convective signature becomes more complex:
223 while MLDs remain relatively deep at the center of the Labrador Sea, they are markedly reduced
224 along the basin boundaries (Fig. 4a). This spatial contraction suggests that while interior
225 convection partially recovers following the period of suppression[80], the inhibition of diapycnal
226 mixing along the basin boundaries—specifically across the pathways of the subpolar boundary
227 current system—may hinder or delay the transport of dense water into the deep boundary
228 current[35,81]. Such localized cessation and retreat of the convective margin via fresh and warm
229 sub-mesoscale flows from the boundary currents during isolated convective events have been
230 documented by recent high-resolution glider observations[82]. Consequently, this potentially limits

231 the volume of dense water available for southward export, explaining why the subpolar anomaly
232 (ΔMOC_{SPO}) remains negative at -1.45 *Sv* despite the recovered interior convection.
233 These modern patterns find historical analogs earlier in the record. The massive suppression
234 of deep convection during 1965–1974 (Fig. 4f)[83]—the most extensive in the historical record—
235 shows a striking resemblance to the 2005–2014 period of suppressed convection (Fig. 4b).
236 Similarly, the MLD anomalies during 1975–1994 (Fig. 4d, e) mirror the MLD shoaling across
237 the basin boundaries during 2015–2022. These earlier periods of weakening (1965–1994) are
238 closely associated with the propagation of Great Salinity Anomalies through the Subpolar Gyre,
239 which stratified the water column and inhibited dense water formation[44,68-71]. Thus, our findings
240 suggest that the recent decline represents a contemporary recurrence of these historical
241 convective suppressions, occurring alongside an eroding northern stability.
242 Notably, this decrease in dense water formation is not limited to the subpolar region. Our
243 results also capture a sustained decline in the intensity of open-ocean convection within the
244 Nordic Seas beginning in 1975–1984 (Fig. 4a–e). Previous studies have attributed this reduction
245 to the wintertime retreat of local sea ice and the associated decrease in brine rejection, combined
246 with diminished surface turbulent heat loss to the atmosphere and consequent anomalous
247 warming[52,53]. The persistence of this northern suppression through 2015–2022 highlights a
248 continuous erosion of the northern buffer, ultimately manifesting as a poleward extension of the
249 AMOC weakening.
250
251 **Downstream weakening and interdecadal shifts of the DWBC.** It is important to note that
252 dense water formation is not solely the product of open-ocean convection; significant water mass
253 transformation also occurs via diapycnal mixing and boundary current cooling across the

subpolar North Atlantic, the northern Nordic Seas, and the Arctic Ocean. Regardless of their diverse regional origins or specific formation mechanisms, these dense water masses ultimately exit the subpolar system via the DWBC and adjacent interior pathways[84,85]. In this sense, the DWBC functions as an important artery of the AMOC's lower limb, integrating these various upstream signals and carrying the collective pulse of the overturning circulation southward. Therefore, to examine how the upstream convective suppressions translate into physical transport, we analyze the meridional velocity anomalies across 45°N (Fig. 5).

The velocity profiles show an overall weakening of the DWBC before and after the 1995-2004 partial recovery period, consistent with AMOC's interdecadal anomalies during the corresponding periods (Figs. 2, 3). They also reveal a critical distinction between the two most recent decades of decline. During 2005–2014 (Fig. 5b), the DWBC weakening is predominantly focused at mid-depths (500–2000 *m*), aligning closely with the core layer of LSW (1000–2500 *m*). This corresponds remarkably well with our earlier findings (Fig. 3) that the deficit in dense water formation during this period of suppressed convection is largely confined to the subpolar region (ΔMOC_{SPO} = -2.63 *Sv*, ΔMOC_{NOR} = -0.51 *Sv*). In contrast, during the 2015–2022 period (Fig. 5a), the DWBC weakening becomes much more robust, spanning nearly the entire deep-water column from 1000 to 4000 *m*. This downward extension of the velocity deficit matches the suppressed sinking in both the subpolar North Atlantic and the northern Nordic Seas (ΔMOC_{SPO} = -1.45 *Sv*, ΔMOC_{NOR} = -1.12 *Sv*). This indicates that during the most recent decade, the DWBC weakening is no longer confined to the LSW core but extends into the deeper overflow waters, namely the Iceland–Scotland Overflow Water and Denmark Strait Overflow Water, typically occupying depths below 2500 *m*[86]. Notably, the DWBC profile during 1975–1994 (Fig. 5d, e) exhibits a similar weakening in the deep overflow layers, mirroring the modern 2015–2022 case.

This physical constriction of the DWBC during 1975–1994 and 2015–2022 is strongly corroborated by the AMOC streamfunction in density space. Specifically, the deepest portion of the AMOC's lower limb ($\rho_2 \gtrsim 1{,}037$ kg m^{-3}) exhibits a corresponding weakening during the respective periods of 1975–1994 and 2015–2022 (Figs. 3, S1). This persistent deep-layer deficit indicates that the southward return flow originating from the Nordic Seas is shifted toward lower density classes during these decades of widespread decline. Crucially, this further reinforces our earlier hypothesis that the AMOC state during 2015–2022 represents a re-emergence of past large-scale disruptions, governed by the same underlying physical mechanisms.

We note that while the advective timescale for water masses to physically travel from the Nordic Seas overflows to the Labrador Sea interior and then into the DWBC at 45°N can span several years to a decade[87-89], the covariability on decadal timescales between the overflows and the DWBC at 45°N could also be mediated by rapid dynamical adjustment. As shown in previous theoretical and modeling studies[90-92], high-latitude buoyancy anomalies excite Kelvin waves and topographic Rossby waves. These baroclinic waves propagate downstream along the continental slope on a much faster timescale, adjusting the downstream geostrophic transport of the DWBC long before the anomalous water masses themselves arrive at the western boundary. Therefore, the covarying signals of the DWBC and the Nordic Seas overflows may reflect this rapid wave-driven boundary adjustment.

Salinity-driven weakening and thermal compensation. While these deficits in the AMOC's deep lower limb and the corresponding constriction of the DWBC characterize the 1975–1994 and 2015–2022 periods, they raise a broader mechanistic question regarding the entire historical record: is the overall weakening of the AMOC relative to the 1955–1964 baseline period

300 primarily driven by temperature or salinity changes? To isolate the relative contributions of these
301 competing buoyancy forcings, we conducted two sets of sensitivity experiments (see Methods).
302 In the first set of experiments, the robust diagnostic model was forced with the actual decadal
303 salinity fields while temperature was held constant at the 1955–1964 baseline state, effectively
304 isolating the salinity effect. In the second set, the robust diagnostic model was forced with the
305 actual decadal temperature fields while holding salinity constant at the baseline state, isolating
306 the thermal effect.

307 The AMOC streamfunction anomalies from these decoupled experiments reveal a stark
308 contrast. When forced by interdecadal salinity changes alone (Figs. 6a-d, S3a, b), the robust
309 diagnostic model reproduces profound, deep-reaching transport deficits that overall resemble the
310 total AMOC decline. In these salinity-isolated scenarios, dense water formation in the subpolar
311 North Atlantic (MOC_{SPO}) and total export at 45°N exhibit large reductions across all periods,
312 including the 1995-2004 partial recovery period (Figs. 6i-l, S3e, f). The salinity-driven
313 weakening is the largest in 1985-1994 and 2015-2022 periods, suggesting that the freshening
314 effect in 2015-2022 is as large as that during the Great Salinity Anomalies of the 1980s and
315 1990s. Conversely, when forced by temperature changes alone (Fig. 6e-h, S3c, d), the isolated
316 thermal forcing acts to increase overturning during the entire 1975–2004 period, serving as a
317 compensatory mechanism. This dynamic tug-of-war is explicitly quantified in the regional
318 transport summaries (Figs. 6i-l, S2e, f). For example, during the 1995–2004 partial recovery
319 period, the isolated salinity forcing drives a large transport deficit at 45°N (by 2.26 *Sv*), which is
320 partially offset by the thermal forcing's attempt to increase dense water formation in the subpolar
321 North Atlantic (+0.55 *Sv*), the northern Nordic Seas (+0.33 *Sv*), and the Arctic Ocean (+0.30 *Sv*)
322 (Fig. 6k).

Crucially, however, a stark reversal emerges during the recent 2005–2022 period. Over these two decades, thermal changes actively suppress the total export at 45°N, abandoning their historical compensatory role. Specifically, the isolated thermal forcing accounts for a 1.48 *Sv* reduction in dense water formation within the subpolar region during 2005–2014 (Fig. 6j) and a 1.16 *Sv* reduction in the northern Nordic Seas during 2015–2022 (Fig. 6i). As a result of this shift, thermal anomalies no longer buffer the salinity-driven decline, but instead act in tandem with it. Ultimately, these sensitivity experiments demonstrate that while the sustained interdecadal weakening of the AMOC remains fundamentally a salinity-driven phenomenon, the recent breakdown of thermal compensation renders the AMOC system increasingly vulnerable to high-latitude freshwater forcing.

To trace the origins of the salinity-driven weakening and the recent reversal of thermal compensation, we further examine the spatial distribution of buoyancy anomalies within the preconditioning layer of the upper 250 *m* (Figs. 7, 8). For open-ocean deep convection to occur, wintertime surface density must increase sufficiently to break through the resulting upper-ocean buoyancy barrier. However, the decadal salinity anomaly fields (Fig. 7) reveal a persistent and widespread accumulation of surface freshwater (negative salinity anomalies) across the western subpolar North Atlantic. This extensive surface freshening during 1965–1994 clearly reflects the successive Great Salinity Anomalies of the 1970s, 1980s, and 1990s[43-48,68-71]. It appears to be well-connected along the pathways of the Greenland–Labrador Current system, pointing toward both Arctic and Greenland origins. This surface freshening pauses during the partial recovery period of 1995–2004, before resuming during 2005–2022 with a strong spatial connection to both source regions (Fig. 7a, b). Additionally, recent studies documented that strong freshening events originating in the eastern Iceland Basin[93] during 2012–2016 propagated into the Irminger

346 Sea and were subsequently advected by the regional boundary currents[94].

347 While this surface freshening creates a highly buoyant surface cap that increases vertical
348 stability and suppresses the formation of LSW, the mechanism by which this surface freshening
349 affects the DWBC is dynamically distinct. Specifically, an increase in surface buoyancy across
350 the Labrador Current directly alters the surface zonal pressure gradient, accelerating the
351 southward surface geostrophic current. At depth, however, the thermal wind relationship dictates
352 that this pressure gradient anomaly reverses because the upper ocean is occupied by anomalously
353 light water compared to the neighboring interior ocean. Consistent with this baroclinic pressure
354 gradient anomaly, the geostrophic flow at depth slows down, manifesting as a reduction in
355 DWBC transport. Our sensitivity experiments explicitly capture this dynamical signature,
356 demonstrating a large-scale, salinity-driven reduction of DWBC transport extending into the
357 deep overflow layers (below 2500 *m*)[86] spanning the entire 1975–2022 period (Fig. S4).

358 During 1975–1994, the freshwater cap is partially mitigated by widespread upper ocean
359 cooling across the western subpolar North Atlantic (Fig. 8d, e). These negative temperature
360 anomalies effectively destabilize the surface waters, helping to erode the freshwater cap and
361 force the open-ocean convective mixing that sustains the compensatory thermal overturning
362 observed in our sensitivity experiments. During the subsequent 1995–2004 partial recovery
363 phase, the upper 250 *m* of the subpolar region exhibits mild warming[73,95], indicating that surface
364 heat loss no longer drives the thermal destabilization. Instead, negative temperature anomalies
365 persist at depth (Fig. S5c), reflecting the residual imprint of the massive cold and fresh LSW
366 layer formed during the early to mid-1990s[72,96-98]. Consequently, it is these deep, fresh, and cold
367 anomalies (Figs. S5c, S6c) that simultaneously sustain the salinity-driven weakening and the
368 compensatory thermal overturning throughout this decade.

Once this deep thermal buffer is slowly depleted (Fig. S5a, b), however, the surface temperature fields for the 2005–2022 period (Fig. 8a, b) reveal why the historical safety net fails. Widespread warming is apparent in the Nordic Seas, Baffin Bay, and along the Labrador Current during the 2005–2014 and 2015–2022 intervals[99,100]. Instead of destabilizing the surface to offset the freshwater influence, this positive temperature anomaly further increases surface buoyancy to interfere with dense water formation. It also accelerates the surface Labrador Current while restricting the DWBC (Fig. S7a, b). Therefore, by working in tandem with the increased freshwater influx, the modern thermal state acts to amplify the surface buoyancy, thus contributing to the DWBC decline.

It is worth noting that while the basin margins and northern seas warm during the 2005–2022 periods, the interior subpolar North Atlantic remains anomalously cold, a feature that becomes particularly pronounced during 2015–2022 (Fig. 8a, b). This localized cooling, which is referred to as the North Atlantic warming hole, is often interpreted as a signature of reduced ocean heat transport associated with a weakened AMOC[16,54,55,57] or a sign of increased deep convection[23]. Regardless of its origin, our findings suggest that this interior cooling is insufficient to overcome the increased stratification established in the Nordic Seas and along the boundary current pathways. Consequently, it fails to offset the broader AMOC decline.

Discussion

In this study, we reconstructed the historical states of the AMOC since the mid-1950s and investigated the drivers of its interdecadal changes using a robust diagnostic ocean model constrained by historical hydrographic observations. Our results suggest that the AMOC's interdecadal evolution from the baseline period of 1955–1964 follows a prolonged weakening

(1965–1994), a brief partial recovery (1995–2004), and then a subsequent steep decline (2005–2022). As such, it cannot be solely characterized by a monotonic (human-induced) decline or interdecadal (natural) variability, but rather by a complex interplay of the two[30,101]. While the 1965–1994 weakening is driven by suppressed dense water formation in the subpolar region, the recent decline (2005–2022) stems from combined reductions across the subpolar North Atlantic and northern Nordic Seas, against a partial, compensating increase within the Arctic Ocean.

According to the sensitivity experiments, in which the salinity- and temperature-driven changes in the AMOC are decoupled, the AMOC decline—both prior to and after the partial recovery period (1995–2004)—is primarily driven by salinity anomalies characterized by spatial patterns that point toward increased freshwater influxes from Arctic export and Greenland ice melt. The magnitude of the freshwater-driven AMOC decline during the recent decades (2005–2022) is on par with that during 1985–1994, the decade coinciding with the Great Salinity Anomalies of the 1980s and 1990s. Collectively, these results suggest that the AMOC system has been operating under a long-term freshening regime since the mid-1960s, manifested by repeated episodes of severe negative salinity anomalies that are broadly, though not exclusively, tied to Arctic export and Greenland ice melt.

However, thermal buffering by a relatively cold state is apparent during 1975–2004. In particular, the transient rebound in 1995–2004 occurs solely because the temperature-driven AMOC anomalies—associated with a massive volume of cold LSW formed during a prolonged, strongly positive phase of the NAO in the preceding years—temporarily mask this freshwater-driven suppression. Following this transient rebound, however, the system seems to cross a critical threshold, marking a breakdown of the thermal buffering in 2005–2022. Widespread warming in the Nordic Seas and along the basin margins now works in tandem with freshwater

influxes to create a highly buoyant surface cap. This combined buoyancy anomaly suppresses dense water formation and drives a baroclinic adjustment that actively curtails southward DWBC transport, ultimately driving the steeper decline of the AMOC in the modern era

It is important to acknowledge the key limitations inherent in our hydrography-based robust diagnostic framework. First, the spatial and temporal coverage of the hydrographic data (World Ocean Atlas 2023, WOA23)[102,103] before the beginning of the Argo era (the early 2000s) is more limited than in recent decades. Because the WOA23 objective analysis scheme fills data-scarce regions by mapping sparse anomalies against a modern-dominated, "all-data" background climatology, historical fields in data-void zones naturally exhibit a structural smoothing toward post-Argo mean conditions. Additionally, the standard Argo floats are fundamentally restricted to the upper 2000 *m* of the water column. Consequently, the vast majority of deep-ocean hydrographic data below 2000 *m* rely on shipboard CTD profiles and deep Argo floats, which remain far scarcer than core Argo observations across all decades. While these well-known baseline constraints in WOA23 are mitigated here by utilizing decadally averaged hydrographic fields, it still represents the primary source of uncertainty in our historical reconstruction for the deep ocean and the pre-Argo era.

Second, while the overall trajectory of AMOC evolution largely agrees with a previous robust diagnostic analysis[29], there are important discrepancies regarding the attribution of the underlying drivers. Previously, the interdecadal AMOC changes during 1955–2017 were attributed to a delayed response to the NAO, a mode of long-term natural climate variability. This conclusion prevailed because the AMOC decline during 2005–2017 (following the 1995–2004 partial recovery) remained relatively weak; consequently, the NAO signal obscured longer-term trends and dominated the interdecadal AMOC evolution. Crucially, our sensitivity

experiments indicate that the NAO is not the overriding driver for the long-term trajectory. They demonstrate that while the strong positive NAO in the early to mid-1990s remains the primary driver of the decadal-scale partial recovery during 1995–2004, the overall AMOC weakening before and after this period is largely driven by a long-term freshening regime, linked to repeated episodes of high-latitude salinity anomalies.

While based on a similar robust diagnostic approach, the previous study used a lower horizontal resolution (1°) ocean model than the 0.25° employed here, along with different numerical configurations and parameterizations. Therefore, we tested the sensitivity of the AMOC reconstruction to horizontal model resolution by performing additional sets of robust diagnostic model simulations using 1° and 0.5° resolutions (see Methods). These experiments show that the AMOC at 45°N weakens by only 0.98 *Sv* over the 2005–2022 period in the 1° resolution case (Fig. S8b, f). This is in line with the previous robust diagnostic study[29]. In the 0.5° resolution case, the AMOC exhibits a much greater weakening of 1.81 *Sv* (Fig. S9b, f), which closely approaches the 2.25 *Sv* reduction in our main results. Interestingly, the compensating role of the Arctic Ocean is generally greater in the lower-resolution cases than in our main results, which is partly responsible for the differences in the extent of AMOC decline. This resolution dependence is likely linked to the representation of the boundary currents, which tend to be more locally balanced and diffusive—and thus less dynamically connected to upstream changes—in the lower-resolution models.

Ultimately, this sensitivity to model resolution and the data sparsity in the deep ocean and during the pre-Argo period serve as an important caveat: the interdecadal AMOC evolution derived from our robust diagnostic framework carries inherent structural uncertainties, and thus should not be viewed as an exact historical trajectory or a substitute for continuous direct

monitoring programs. Rather, it stands as a complementary tool that helps estimate and resolve long-term AMOC changes, while clarifying the complex physical processes driving them.

Finally, based on the findings and insights gained from our robust diagnostic framework, the evolution of the AMOC over the next decade will serve as a crucial test of its near-term trajectory. One possibility is that the system will continue to decline under sustained high-latitude freshening and warming. Alternatively, the enhanced subpolar deep convection documented during the recent period could trigger a delayed, partial recovery of the AMOC, mirroring the temporary stabilization that occurred during 1995–2004. The uncertainty surrounding these contrasting pathways underscores the critical importance of maintaining sustained ocean observations to closely monitor which trajectory the AMOC system will take.

Methods

Data and model used. In this study, we carried out a series of global ocean and sea-ice model simulations with the model temperature and salinity fields constrained by the 0.25° resolution World Ocean Atlas 2023 climatology (WOA23)[102,103], an approach often referred to as robust diagnostic model simulations[104]. These simulations were conducted using the Modular Ocean Model version 6 (MOM6) and the Sea Ice Simulator version 2 (SIS2.0) from the Geophysical Fluid Dynamics Laboratory[22], and were driven by surface forcing fields derived from the European Centre for Medium-Range Weather Forecasts reanalysis-5 (ERA5)[105]. Both the ocean and sea-ice model components have a nominal horizontal resolution of 0.25°, comprising 1,440 zonal and 1,080 meridional grid cells globally. This configuration utilizes a Mercator grid across the tropics and extra-tropics, a bipolar grid northward of approximately 64°N, a spherical grid between roughly 67°S and 78°S, and a displaced pole grid southward of 78°S. The ocean model

has 75 layers in an isopycnal-z* hybrid vertical coordinate system.

Robust diagnostic model simulations. To reconstruct the AMOC and its interdecadal changes since the mid-1950s, the model temperature and salinity fields were relaxed to WOA23 for each target period between 1955 and 2022 (i.e., 1955–1964, 1965–1974, 1975–1984, 1985–1994, 1995–2004, 2005–2014, and 2015–2022). Our robust diagnostic framework computes ocean circulation fields that are dynamically consistent with these historical hydrographic fields. As such, it is not designed to explicitly simulate fully transient physical processes; instead, it relies on geostrophic balance and mass continuity—constrained by long-term averaged hydrography—to diagnose ocean circulation, water mass transformations, and the resulting decadal AMOC states. Each simulation was integrated for 50 years. For the initial cycle of integration, the surface flux fields were prescribed sequentially from the corresponding historical years (e.g., a 10-year loop for the full decades, or an 8-year loop for the 2015–2022 period). This forcing cycle was then repeated periodically through year 50.

All simulations approached their respective equilibrium states after the first cycle. To account for model spin-up and to ensure the deep ocean reached a robust equilibrium, the first 20 years of integration were discarded, and the outputs from the final 30 years were time-averaged for the analysis. Because the temperature and salinity fields were relaxed to the decadal climatologies throughout the integration, internal ocean variability is heavily suppressed. Consequently, the final 30 years represent a largely deterministic equilibrium state forced by the climatological temperature and salinity fields and the repeating atmospheric cycle, rendering traditional statistical significance tests against internal ocean variability inapplicable in our experimental design.

507

508 **AMOC streamfunction in density coordinates and region definitions.** To capture the full
509 overarching structure of the overturning circulation and its high-latitude variability, the AMOC
510 streamfunction (Ψ) is calculated by integrating the meridional velocity zonally across the
511 Atlantic–Arctic basin in potential density space referenced to 2000 *dbar*, from the ocean floor
512 upward to a specific potential density (ρ_2) surface:

513 $$\Psi(y, \rho_2) = -\int_{\rho_2}^{\rho_2^{\max}} \int_{x_e}^{x_w} v \, dx d\rho_2 \quad (1)$$

514 where x_w and x_e represent the western and eastern boundaries of the Atlantic–Arctic basin, and
515 $\rho_2^{\max}$ is the maximum density at the ocean floor. The strength of the AMOC at specific latitudes
516 is defined as the maximum value of this streamfunction.

517 While the vast majority of previous observational and reanalysis studies evaluate high-
518 latitude overturning transport (e.g., across the Greenland–Scotland Ridge, Fram Strait, and
519 Barents Sea) using surface-referenced potential density (ρ_0)[32,35-39,41], our framework intentionally
520 utilizes ρ_2. At the near-freezing temperatures characteristic of high-latitude regions, the thermal
521 expansion coefficient of seawater approaches zero at the surface. Therefore, when using ρ_0,
522 distinct intermediate, overflow, and deep-water masses collapse into a narrow range of density
523 classes. When the velocity field is integrated across these compressed layers, overlapping
524 northward and southward flow components suffer a degree of numerical cancellation, which
525 artificially diminishes the diagnosed baroclinic shear. By referencing potential density to 2000
526 *dbar* (ρ_2), the thermobaric effects inherent to the non-linear equation of state expand the density
527 coordinate spectrum for these cold, dense water masses. This reference frame effectively
528 prevents artificial transport cancellation within the streamfunction integration, providing a more
529 physically robust representation of the true maximum overturning intensity across the high-

latitude passages. Indeed, a direct sensitivity test using our model data demonstrates that calculating the AMOC streamfunction at 70°N in ρ_0 space results in an overturning transport that is approximately 1–2 *Sv* weaker than that calculated in ρ_2 space. Consequently, we caution that a direct comparison of our absolute overturning transport values with those from previous ρ_0-based studies is subject to systematic offsets inherent to the choice of vertical coordinate.

To quantify the rate of net diapycnal sinking within specific regional basins, we calculate the difference in maximum overturning transport between their respective latitudinal boundaries. This defines the diapycnal sinking rates for the subpolar North Atlantic between 45°N and 70°N ($MOC_{SPO} = MOC_{45N} - MOC_{70N}$), the northern Nordic Seas between 70°N and 80°N ($MOC_{NOR} = MOC_{70N} - MOC_{80N}$), and the Arctic Ocean poleward of 80°N ($MOC_{ARC} = MOC_{80N}$). Under this sign convention, net diapycnal sinking within each basin is defined as positive. For the hydrographic analysis, the Labrador Sea Water (LSW) layer is defined by the vertical depth range of 1000–2500 *m* across the subpolar North Atlantic.

Optimization of the robust diagnostic model. While the original robust diagnostic framework[104] employed relatively strong damping (i.e., an e-folding timescale of less than one year) to derive steady-state ocean circulations, such aggressive relaxation can over-constrain internal model physics and introduce unphysical heat and salt sources/sinks. To explore interdecadal changes in large-scale circulation without over-constraining the model's internal dynamics, a much less restrictive constraint is required. To determine an optimal temperature and salinity relaxation coefficient, we carried out several tuning experiments. In agreement with an earlier study[59], the spatial pattern and strength of the AMOC became unrealistic when the relaxation coefficient was set below an e-folding time of ~3 years, whereas interdecadal changes

553 in temperature and salinity in the high-latitude North Atlantic significantly deviated from those
554 of WOA23 when the relaxation coefficient was increased beyond an e-folding time of ~10 years.
555 Therefore, an e-folding time of 5 years was applied to relax the model temperature and salinity
556 toward WOA23 for the entire water column. For the surface layer, the e-folding time scales
557 proportionally with layer thickness, equivalent to 30 days per 10 *m*.
558 However, initial model results yielded a maximum AMOC transport across 26.5°N that was
559 much weaker than direct observations from the RAPID array[106] (Fig. S10a). Additionally, the
560 southward return flow of dense water ($\sigma_0 \gtrsim 27.5\ kg\ m^{-3}$) from the Nordic Seas across the OSNAP
561 array was significantly underestimated compared to observations[107] (Fig. S10d). These
562 deficiencies are largely due to the model's horizontal resolution (0.25°), which is inherently
563 insufficient for fully resolving the narrow, deep overflow currents across the Denmark Strait and
564 Faroe-Bank Channel[21,22]. To circumvent this critical shortcoming, we modified the topography
565 within the Denmark Strait and Faroe-Bank Channel. Specifically, the Denmark Strait was
566 deepened from ~600 *m* to 900 *m*, and the Faroe-Bank Channel from ~900 *m* to 1000 *m*. Both
567 channels were also widened to ensure a minimum of four grid points across each passage.
568 Following this topographic adjustment, the modeled AMOC transport achieved reasonable
569 agreement with direct observations across the RAPID and OSNAP arrays (Fig. S11). These
570 topographic adjustments, combined with the selections of optimal relaxation coefficients, allow
571 us to reconstruct interdecadal AMOC changes that are consistent with hydrographic observations
572 while maintaining a physically realistic AMOC state.
573
574 **Sensitivity experiments**. In addition to the primary set of robust diagnostic model simulations,
575 we carried out four sets of sensitivity experiments. The first two sets were designed to isolate the

relative contributions of salinity-driven versus temperature-driven buoyancy forcing to the AMOC's interdecadal changes. In the first set, the model salinity fields were relaxed to the actual decadal salinity fields from WOA23, while the model temperature fields were relaxed to the 1955–1964 baseline state. For example, S2015:T1955 denotes the experiment constrained by 2015–2022 salinity and 1955–1964 temperature. In the second set, the model temperature fields were relaxed to the actual decadal temperature fields, while the model salinity fields were relaxed to the 1955–1964 baseline state (e.g., T2015:S1955, for example, denotes the experiment constrained by 2015–2022 temperature and 1955–1964 salinity). Note that due to the nonlinearity of the seawater equation of state, the linear sum of these isolated experiments does not fully account for the total anomaly, with the remaining variance attributed to nonlinear interaction terms. In this study, we focus on these isolated components to quantify their primary contributions to the AMOC's interdecadal changes.

The remaining two sensitivity experiments were designed to evaluate the impact of the model's horizontal resolution on the reconstructed AMOC and its interdecadal changes, helping to reconcile the key discrepancies between the current findings and a previous study[29]. These resolution sensitivity experiments were identical to the primary set of robust diagnostic model simulations, but were conducted using lower horizontal resolution configurations at 1° and 0.5° (Figs. S8, S9).

Data availability

The World Ocean Atlas 23 (WOA23) data were downloaded from NOAA's National Centers for Environmental Information at https://www.ncei.noaa.gov/access/world-ocean-atlas-2018. The European Centre for Medium-Range Weather Forecasts (ECMWF) reanalysis-5

(ERA5) surface flux data were downloaded from the Copernicus Climate Change Service at https://cds.climate.copernicus.eu/datasets/reanalysis-era5-single-levels. All other data used in this study will be made available at https://www.ncei.noaa.gov before the publication.

Code availability

The code of the Modular Ocean Model version 6 (MOM6) and the Sea Ice Simulator version 2 (SIS2.0) is publicly available from the public GitHub repository at https://github.com/NOAA-GFDL/MOM6.

Acknowledgements

The authors thank Leah Chomiak for helpful discussion and insightful comments. This work was supported by the base funding of NOAA's Atlantic Oceanographic and Meteorological Laboratory (AOML). F.A.G. was supported by the Northern Gulf Institute under NOAA cooperative agreement NA21OAR4320190. D.K was supported by NOAA's AOML in part under the auspices of the Cooperative Institute for Marine and Atmospheric Studies (CIMAS), a cooperative institute of the University of Miami and NOAA, cooperative agreement NA20OAR4320472.

Author contributions

S-K.L. conceived the study, performed the analysis and wrote the initial draft of the paper. S-K.L. carried out the hydrography-constrained robust diagnostic ocean & sea-ice model simulations. F.A.G. and D.K. assisted the model simulations. All authors (S-K.L., F.A.G., D.K.,

H.L., S.D., and R.L.) significantly contributed to the discussion and interpretation of results, and reviewed and edited the paper.

Competing interests

The authors declare no competing interests.

References

1. Gregory, J. M., et al. A model intercomparison of changes in the Atlantic thermohaline circulation in response to increasing atmospheric CO2 concentration. *Geophys. Res. Lett.* **32**, L12703 (2005).
2. Schmittner, A., Latif, M., & Schneider, B. Model projections of the North Atlantic thermohaline circulation for the 21st century assessed by observations. *Geophys. Res. Lett.* **32**, L23710 (2005).
3. Weaver, A. J., et al. Stability of the Atlantic meridional overturning circulation: A model intercomparison, *Geophys. Res. Lett.* **39**, L20709 (2012).
4. Cheng, W., et al. Atlantic meridional overturning circulation (AMOC) in CMIP5 models: RCP and historical simulations. *J. Clim.* **26**, 7187-7197 (2013).
5. Weijer, W., Cheng, W., Garuba, O. A., Hu, A. & Nadiga, B. T. CMIP6 models predict significant 21st century decline of the Atlantic meridional overturning circulation. *Geophys. Res. Lett*. **47**, e2019GL086075 (2020).
6. Schmittner, A. Decline of the marine ecosystem caused by a reduction in the Atlantic overturning circulation. *Nature* **434**, 628–633 (2005).
7. Boot, A. A., Steenbeek, J., Coll, M., von der Heydt, A. S., & Dijkstra, H. A. Global marine

ecosystem response to a strong AMOC weakening under low and high future emission scenarios. *Earth's Future* **13**, e2024EF004741 (2025).

8. Little, C. M. et al. The Relationship between U.S. East Coast sea level and the Atlantic meridional overturning circulation: a review. *J. Geophys. Res. Oceans* **24**, 6435–6458 (2019).

9. Kim, D. et al. Dynamically downscaled future projections of the Northwest Atlantic Ocean across low to high emissions scenarios. *Ocean Sci*. **22**, 1987–2009 (2026).

10. Lopez, H., Dong, S., Lee, S.-K., & Goni, G. Decadal modulations of interhemispheric global atmospheric circulations and monsoons by the South Atlantic meridional overturning circulation. *J. Clim.* **29**, 1831–1851 (2016).

11. Ben-Yami et al. Impacts of AMOC collapse on monsoon rainfall: A multi-model comparison. *Earth's Future* **12**, e2023EF003959 (2024).

12. Zhang, R. et al. A review of the role of the Atlantic meridional overturning circulation in Atlantic multidecadal variability and associated climate impacts. *Rev. Geophys*. **57**, 316–375 (2019).

13. Cunningham, S. A. et al. Temporal variability of the Atlantic meridional overturning circulation at 26.5°N. *Science* **317**, 935-938 (2007).

14. Lozier, S. M. et al. Overturning in the Subpolar North Atlantic Program: A New International Ocean Observing System. *Bull. Amer. Meteor. Soc*. **98**, 737–752 (2017).

15. Kersalé, M. et al. Highly variable upper and abyssal overturning cells in the South Atlantic. *Sci. Adv*., **6**, eaba7573 (2020).

16. Rahmstorf, S. et al. Exceptional twentieth-century slowdown in Atlantic Ocean overturning circulation. *Nat. Clim. Change* **5**, 475–480 (2015).

17. Caesar, L., Rahmstorf, S., Robinson, A., Feulner, G. & Saba, V. Observed fingerprint of a weakening Atlantic Ocean overturning circulation. *Nature* **556**, 191–196 (2018).

18. Caesar, L., McCarthy, G. D., Thornalley, D. J. R., Cahill, N. & Rahmstorf, S. Current Atlantic Meridional Overturning Circulation weakest in last millennium. *Nat. Geosci*. **14**, 118–120 (2021).

19. Danabasoglu, G. et al. North Atlantic simulations in Coordinated Ocean-ice Reference Experiments phase II (CORE-II). Part II: Interannual to decadal variability. *Ocean Model.* **97**, 65–90 (2016).

20. Tsujino, H. et al. Evaluation of global ocean–sea-ice model simulations based on the experimental protocols of the Ocean Model Intercomparison Project phase 2 (OMIP-2). *Geosci. Model Dev.* **13**, 3643–3708 (2020).

21. Chang, Y. S., Garraffo, Z. D., Peters, H., & Özgökmen, T. M. Pathways of Nordic Overflows from climate model scale and eddy resolving simulations. *Ocean Model.* **29**, 66-84 (2009).

22. Adcroft, A. et al. The GFDL global ocean and sea ice model OM4.0: Model description and simulation features. *J. Adv. Model. Earth Syst*, 11 (2019).

23. de Jong, M. F., & de Steur, L. Strong winter cooling over the Irminger Sea in winter 2014–2015, exceptional deep convection, and the emergence of anomalously low SST, *Geophys. Res. Lett*. **43**, 7106–7113 (2016).

24. Kim, W. M., Yeager, S., & Danabasoglu, G. Revisiting the causal connection between the Great Salinity Anomaly of the 1970s and the shutdown of Labrador Sea deep convection. *J. Clim.*, **34**, 675–696 (2021).

25. Worthington, E. L. et al. A 30-year reconstruction of the Atlantic meridional overturning circulation shows no decline. *Ocean Sci.* **17**, 285–299 (2021).

690 26. Caínzos, V. et al. Thirty years of GOSHIP and WOCE data: Atlantic Overturning of mass,
691 heat, and freshwater transport. *Geophys. Res. Lett*. **49**, e2021GL096527 (2022).
692 27. Jackson, L. C. et al. The evolution of the North Atlantic meridional overturning circulation
693 since 1980. *Nat. Rev. Earth Environ*. **3**, 241–254 (2022).
694 28. Latif, M., Sun, J., Visbeck, M. Bordbar, M. H. Natural variability has dominated Atlantic
695 meridional overturning circulation since 1900. *Nat. Clim. Change* **12**, 455–460 (2022).
696 29. Lee, S.-K. et al. Human-induced changes in the global meridional overturning circulation are
697 emerging from the Southern Ocean. *Commun. Earth Environ*. **4**, 69 (2023).
698 30. Lee, S.-K. et al. A pause in the weakening of the Atlantic meridional overturning circulation
699 since the early 2010s. *Nat. Commun*. **15**, 10642 (2024).
700 31. Terhaar, J., Vogt, L. & Foukal, N. P. Atlantic overturning inferred from air-sea heat fluxes
701 indicates no decline since the 1960s. *Nat. Commun*. **16**, 222 (2025).
702 32. Lozier, M. S. et al. A sea change in our view of overturning in the subpolar North Atlantic.
703 *Science* **363**, 516-521 (2019).
704 33. Pickart, R. S., Spall, M. A., Ribergaard, M. S., Moore, G. W. K. & Milliff, R. F. Deep
705 convection in the Irminger Sea forced by the Greenland tip jet. *Nature* **424**, 152–156 (2003).
706 34. Chafik, L., & Rossby, T. Volume, heat, and freshwater divergences in the subpolar North
707 Atlantic suggest the Nordic Seas as key to the state of the meridional overturning circulation.
708 *Geophys. Res. Lett*. **46**, 4799–4808 (2019).
709 35. Le Bras, I. A.-A., Straneo, F., Holte, J., de Jong, M. F. & Holliday, N. P. Rapid export of
710 waters formed by convection near the Irminger Sea's western boundary. *Geophys. Res. Lett*.
711 **47**, e2019GL085989 (2020).
712 36. Petit, T., Lozier, M. S., Josey, S. A. & Cunningham, S. A. Atlantic deep water formation

occurs primarily in the Iceland Basin and Irminger Sea by local buoyancy forcing. *Geophys. Res. Lett*. **47**, e2020GL091028 (2020).

37. Zhang, R. & Thomas, M. Horizontal circulation across density surfaces contributes substantially to the long-term mean northern Atlantic meridional overturning circulation. *Commun. Earth Environ*. **2**, 112 (2021).

38. Chafik, L., Holliday, N. P., Bacon, S. & Rossby, T. Irminger Sea is the center of action for subpolar AMOC variability. *Geophys. Res. Lett*. **49**, e2022GL099133 (2022).

39. Koman, G., Johns, W. E., Houk, A., Houpert, L., & Li, F. Circulation and overturning in the eastern North Atlantic subpolar gyre. *Prog. Oceanogr*. **208**, 102884 (2022).

40. Weijer, W. et al. Interactions between the Arctic Mediterranean and the Atlantic meridional overturning circulation: A review. *Oceanogr.* **35**, 118–127 (2022).

41. Årthun, M. et al. Atlantification drives recent strengthening of the Arctic overturning circulation. *Sci. Adv*.11, eadu1794 (2025).

42. Dörr, J. et al. The Arctic overturning circulation: transformations, pathways and timescales, *Ocean Sci.* 22, 565–585, (2026).

43. Aagaard, K., & Carmack, E. C. The role of sea ice and other fresh water in the Arctic circulation. *J. Geophys. Res*. **94**, 14485–14498 (1989).

44. Häkkinen, S. An Arctic source for the great salinity anomaly: A simulation of the Arctic ice-ocean system for 1955–1975. *J. Geophys. Res*. **98**, 16397–16410 (1993).

45. Curry, R. & Mauritzen, C. Dilution of the northern North Atlantic Ocean in recent decades. *Science* **308**,1772-1774 (2005).

46. Yang, Q. et al. Recent increases in Arctic freshwater flux affects Labrador Sea convection and Atlantic overturning circulation. *Nat. Commun*. **7**, 10525 (2016).

736 47. Bamber, J. L. et al. Land ice freshwater budget of the Arctic and North Atlantic Oceans: 1.
737 Data, methods, and results. *J. Geophys. Res. Oceans* **123**, 1827–1837 (2018).
738 48. Zhang, J. et al. Labrador Sea freshening linked to Beaufort Gyre freshwater release. *Nat.*
739 *Commun*. **12**, 1229 (2021).
740 49. Bretones, A., Nisancioglu, K. H., Jensen, M. F., Brakstad, A. & Yang, S. Transient increase
741 in Arctic deep-water formation and ocean circulation under sea ice retreat. *J. Clim.* **35**, 109–
742 124 (2022).
743 50. Otosaka, I. N. et al. Mass balance of the Greenland and Antarctic ice sheets from 1992 to
744 2020. *Earth Syst. Sci. Data* **15**, 1597–1616 (2023).
745 51. Igneczi, A. & Bamber, J. L. A high-resolution pan-Arctic meltwater discharge dataset from
746 1950 to 2021. *Earth Syst. Sci. Data* **17**, 3203–3218 (2025).
747 52. Moore, G. W. K., Våge, K., Pickart, R. S. & Renfrew, I. A. Decreasing intensity of open-
748 ocean convection in the Greenland and Iceland seas. *Nat. Clim. Change* **5**, 877-882 (2015).
749 53. Våge, K. et al. Water mass transformation in the Iceland Sea: Contrasting two winters
750 separated by four decades. *Deep-Sea Res. I: Oceanogr. Res. Pap.* **186**, 103824 (2022).
751 54. Drijfhout, S., van Oldenborgh, G. J., & Cimatoribus, A. Is a decline of AMOC causing the
752 warming hole above the North Atlantic in observed and modeled warming patterns? *J. Clim.*
753 **25**, 8373–8379 (2012).
754 55. Rahmstorf, S. et al. Multidecadal Atlantic “warming hole” heat content variations are caused
755 by ocean heat transport, not by surface fluxes. *Geophys. Res. Lett*. **53**, e2025GL118383
756 (2026).
757 56. Robson, J., Ortega, P., & Sutton, R. A reversal of climatic trends in the North Atlantic since
758 2005. *Nat. Geosci*. **9**, 513–517 (2016).

57. Chemke, R., Zanna, L., & Polvani, L. M. Identifying a human signal in the North Atlantic warming hole. *Nat. Commun*. 11, 1540 (2020).

58. Fan, Y., Chan, D., Clothiaux, E. E., Zhang, P., & Laifang, Li. Subpolar North Atlantic cooling reinforced by colder, drier atmosphere with a weakening Atlantic meridional overturning circulation. *Sci. Adv*. **11**, eads1624 (2025)

59. Lee, S.-K. et al. Global meridional overturning circulation inferred from a data constrained ocean & sea-ice model. *Geophys. Res. Lett*. **46**, 1521–1530 (2019).

60. Goossen, B. W. A benchmark for the environment: big science and 'artificial' geophysics in the global 1950s. J. *Glob. His.* **15**, 149–168 (2020).

61. Speer, K., & Tziperman, E. Rates of water mass formation in the North Atlantic Ocean. *J. Phys. Oceanogr.* **22**, 93–104 (1992).

62. Smethie, W. M., & Fine, R. A. Rates of North Atlantic Deep Water formation calculated from chlorofluorocarbon inventories. *Deep-Sea Res. I: Oceanogr. Res. Pap*. **48**, 189–215 (2001).

63. Østerhus, S. et al. Arctic Mediterranean exchanges: a consistent volume budget and trends in transports from two decades of observations. *Ocean Sci*. **15**, 379–399 (2019).

64. LeBel, D.A. et al. The formation rate of North Atlantic Deep Water and Eighteen Degree Water calculated from CFC-11 inventories observed during WOCE. *Deep-Sea Res. I: Oceanogr. Res. Pap.* **55**, 891-910 (2008).

65. Rossby, T., Flagg, C., Chafik, L., Harden, B., & Søiland, H. A direct estimate of volume, heat, and freshwater exchange across the Greenland-Iceland-Faroe-Scotland Ridge. *J. Geophys. Res. Oceans* **123**, 7139–7153 (2018).

66. Beszczynska-Möller, A., Fahrbach, E., Schauer, U., & Hansen, E. Variability in Atlantic

water temperature and transport at the entrance to the Arctic Ocean, 1997–2010. *ICES J. Mar. Sci*. **69**, 852-863 (2012).

67. Smedsrud, L. H., Ingvaldsen, R., Nilsen, J. E. Ø., & Skagseth, Ø.: Heat in the Barents Sea: transport, storage, and surface fluxes. *Ocean Sci.* **6**, 219–234 (2010).

68. Dickson, R. R., Meincke, J., Malmberg, S. A., & Lee, A. J. The "great salinity anomaly" in the northern North Atlantic 1968–1982. *Prog. Oceanogr.* **20**, 103-151 (1998).

69. Belkin, I. M., Levitus, S., Antonov, J., & Malmberg, S. A. "Great salinity anomalies" in the North Atlantic. *Prog. Oceanogr*. **41**, 1-68 (1998).

70. Belkin, I. M. Propagation of the "Great Salinity Anomaly" of the 1990s around the northern North Atlantic. *Geophys. Res. Lett*. **31**, L08306 (2004).

71. Gelderloos, R., Straneo, F. and Katsman, C. A. Mechanisms behind the temporary shutdown of deep convection in the Labrador Sea: Lessons from the Great Salinity Anomaly years 1968–71. *J. Clim*. **25**, 6743-6755 (2012).

72. Yashayaev, I. Hydrographic changes in the Labrador Sea, 1960−2005. *Prog. Oceanogr*. **73**, 242–276 (2007).

73. Yang, C., Masina, S., Bellucci, A., & Storto, A. The rapid warming of the North Atlantic Ocean in the mid-1990s in an eddy-permitting ocean reanalysis (1982–2013). *J. Clim*. **29**, 5417–5430 (2016).

74. Rhein, M., Steinfeldt, R., Kieke, D., Stendardo, I., & Yashayaev, I. Ventilation variability of Labrador Sea Water and its impact on oxygen and anthropogenic carbon: a review. *Philos. Trans. A Math. Phys. Eng. Sci*. 375, 20160321 (2017).

75. Yeager, S. et al. An outsized role for the Labrador Sea in the multidecadal variability of the Atlantic overturning circulation. *Sci. Adv.* **7**, eabh3592 (2021).

76. Böning, C. W. et al. Decadal changes in Atlantic overturning due to the excessive 1990s Labrador Sea convection. *Nat. Commun.* **14**, 4635 (2023).

77. Pickart, R. S., & Spall, M. A. Impact of Labrador Sea convection on the North Atlantic meridional overturning circulation. *J. Phys. Oceanogr.* **37**, 2207–2227 (2007).

78. Zou, S., Lozier, M. S., Li, F., Abernathey, R., & Jackson, L. Density-compensated overturning in the Labrador Sea. *Nat. Geosci*. **13**, 121–126 (2020).

79. Yashayaev, I. & Loder, J. W. Recurrent replenishment of Labrador Sea Water and associated decadal-scale variability. *J. Geophys. Res. Oceans* **121**, 8095–8114 (2016).

80. Yashayaev, I. Intensification and shutdown of deep convection in the Labrador Sea were caused by changes in atmospheric and freshwater dynamics. *Commun. Earth Environ.* **5**, 156 (2024).

81. Straneo, F. On the connection between dense water formation, overturning, and poleward heat transport in a convective basin. *J. Phys. Oceanogr*. **36**, 1822–1840 (2006).

82. Clément, L., Frajka-Williams, E., von Oppeln-Bronikowski, N., Goszczko, I., & de Young, B. Cessation of Labrador Sea convection triggered by distinct fresh and warm (sub)mesoscale flows. *J. Phys. Oceanogr.* **53**, 1959–1977 (2023).

83. Lazier, J. R. N. Oceanographic conditions at ocean weather ship Bravo, 1964–1974. *Atmos.–Ocean* **18**, 227–238 (1980).

84. Bower, A. S., Lozier, M. S., Gary, S. F., & Böning, C. W. Interior pathways of the North Atlantic meridional overturning circulation. *Nature* **459**, 243–247 (2009).

85. Lozier, S. M., Deconstructing the conveyor belt. *Science* **328**, 1507-1511 (2010).

86. Pickart, R. S. Water mass components of the North Atlantic deep western boundary current. *Deep-Sea Res. I: Oceanogr. Res. Pap* **39**, 1553-1572 (1992).

87. Smith, J. N., Jones, E. P., Moran, S. B., Smethie Jr., W. M., & Kieser. W. E. Iodine 129/CFC 11 transit times for Denmark Strait Overflow Water in the Labrador and Irminger Seas. *J. Geophys. Res.* **110**, C05006 (2005).

88. Chomiak, L. N., Yashayaev, I., Volkov, D. L., Schmid, C., & Hooper, J. A. Inferring advective timescales and overturning pathways of the Deep Western Boundary Current in the North Atlantic through Labrador Sea Water advection. *J. Geophys. Res. Oceans* **127**, e2022JC018892 (2022).

89. Le Bras, I. A.-A. Labrador Sea water spreading and the Atlantic meridional overturning circulation. *Phil. Trans. R. Soc. A* **381**, 20220189 (2023).

90. Kawase, M., Establishment of deep ocean circulation driven by deep-water production. *J. Phys. Oceanogr*. **17**, 2294–2317 (1987).

91. Johnson, H. L., & Marshall, D. P. A Theory for the surface Atlantic response to thermohaline variability. *J. Phys. Oceanogr.* **32**, 1121–1132 (2002).

92. Zhang, R. Latitudinal dependence of Atlantic meridional overturning circulation (AMOC) variations. *Geophys. Res. Lett.* **37**, L16703 (2010).

93. Holliday, N. P. et al. Ocean circulation causes the largest freshening event for 120 years in eastern subpolar North Atlantic. *Nat. Commun*. **11**, 585 (2020).

94. Biló, T. C., Straneo, F., Holte, J., & Le Bras, I. A.-A. Arrival of new Great Salinity Anomaly weakens convection in the Irminger Sea. *Geophys. Res. Lett*. **49**, e2022GL098857 (2022).

95. Robson, J., Sutton, R., Lohmann, K., Smith, D., & Palmer, M. D., Causes of the rapid warming of the North Atlantic Ocean in the mid-1990s. *J. Clim.* **25**, 4116–4134 (2012).

96. Curry, R., McCartney, M. & Joyce, T. Oceanic transport of subpolar climate signals to mid-depth subtropical waters. *Nature* **391**, 575–577 (1998).

97. Molinari, R. L. et al. The arrival of recently formed Labrador Sea Water in the deep western boundary current at 26.5 N. *Geophys. Res. Lett*. **25**, 2249-2252 (1998).

98. Chomiak, L. N., Volkov, D. L., Johns, W. E., Hooper, J. A., & Smith, R. H. Deep ocean cooling and freshening from Subpolar North Atlantic reaches Subtropics at 26.5°N. *Commun. Earth Environ*. **6**, 235 (2025).

99. Tsubouchi, T. et al. Increased ocean heat transport into the Nordic Seas and Arctic Ocean over the period 1993–2016. *Nat. Clim. Chang*. **11**, 21–26 (2021).

100. Ballinger, T. J. et al. Abrupt northern Baffin Bay autumn warming and sea-ice loss since the turn of the twenty-first century. *Geophys. Res. Lett*. **49**, e2022GL101472 (2022).

101. Delworth, T. L. & Zeng, F. The impact of the North Atlantic Oscillation on climate through its influence on the Atlantic meridional overturning circulation. *J. Clim*. **29**, 941–962 (2016).

102. Locarnini, R. A., et al. World Ocean Atlas 2023, Volume 1: Temperature. A. Mishonov Technical Editor, NOAA Atlas NESDIS 89 (2024).

103. Reagan, J. R. et al. World Ocean Atlas 2023, Volume 2: Salinity. A. Mishonov, Technical Editor, NOAA Atlas NESDIS 90 (2024).

104. Sarmiento, J. L., & Bryan, K. An ocean transport model for the North Atlantic. *J. Geophys. Res*. **87**, 394–408 (1982).

105. Hersbach, H. et al. The ERA5 global reanalysis. *Q. J. R. Meteorol. Soc*. **146**, 1999–2049 (2020).

106. Moat B. I. et al. Atlantic meridional overturning circulation observed by the RAPID-MOCHA-WBTS (RAPID-Meridional Overturning Circulation and Heatflux Array-Western Boundary Time Series) array at 26N from 2004 to 2024 (v2024.1a), British Oceanographic Data Centre - Natural Environment Research Council, UK (2026).

874 107. Fu, Y. et al. Characterizing the interannual variability of North Atlantic subpolar
875 overturning. *Geophys. Res. Lett*. **52**, e2025GL114672 (2025).

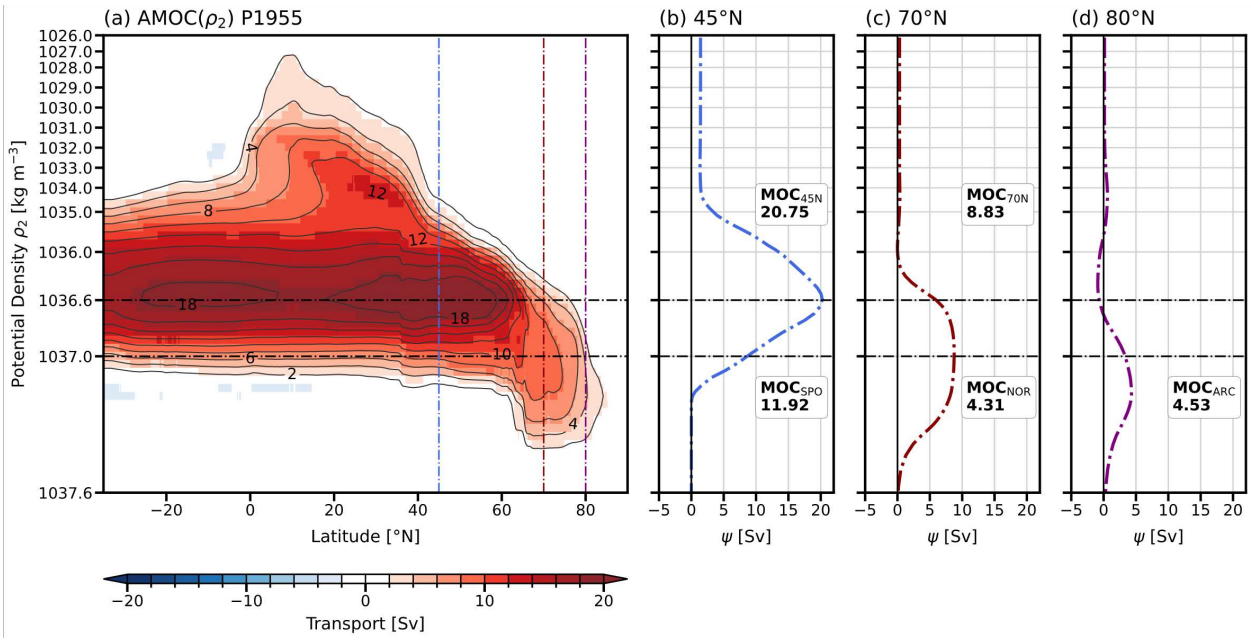


Figure 1. **Baseline AMOC state and regional components**. (a) Total AMOC streamfunction in potential density (ρ_2) coordinates against latitude for the 1955–1964 baseline period. (b–d) Profiles of the AMOC in ρ_2 across 45°N, 70°N, and 80°N. Regional maximum AMOC transport values across 45°N and 70°N (MOC_{45N}, MOC_{70N}), and the rates of sinking in the broader subpolar North Atlantic between 45°N and 70°N (MOC_{SPO}), the northern Nordic Seas between 70°N and 80°N (MOC_{NOR}), and the Arctic Ocean poleward of 80°N (MOC_{ARC}) are indicated within the profiles (see Methods). P1955 denotes the 1955–1964 baseline period. The vertical dash-dot lines in (a) indicate 45°N, 70°N, and 80°N latitudes, while the horizontal dash-dot lines in (a) indicate two ρ_2 isopycnal horizons (1036.6, and 1037 $kg\ m^{-3}$) that roughly demarcate the boundaries between the AMOC's upper and lower limbs, and between the lower limb and the Nordic Seas overflow waters, respectively.

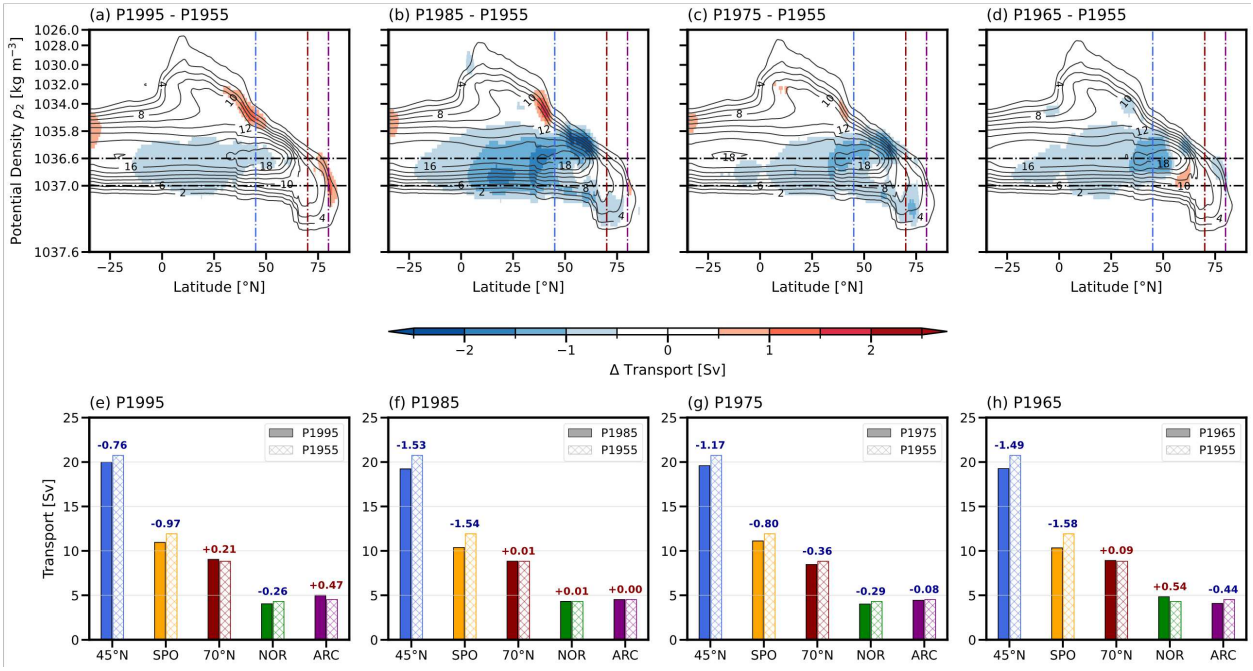


Figure 2. **Decadal AMOC streamfunction anomalies and regional transport summaries for 1965–2004**. (a–d) AMOC streamfunction anomalies in potential density (ρ_2) coordinates against latitude for **a** 1995–2004, **b** 1985–1994, **c** 1975–1984, and **d** 1965–1974 periods relative to the 1955–1964 baseline period. (e–h) Corresponding bar plots summarizing the absolute transport values for regional MOC components (MOC_{45N}, MOC_{SPO}, MOC_{70N}, MOC_{NOR}, and MOC_{ARC}) compared to the baseline period (hatched bars). Analysis periods are denoted by their initial boundary years (e.g., P1955 represents the 1955–1964 baseline, P1965 represents 1965–1974, and P1995 represents 1995–2004). The vertical dash-dot lines in (a–d) indicate 45°N, 70°N, and 80°N latitudes, while the horizontal dash-dot lines in (a–d) indicate two ρ_2 isopycnal horizons (1036.6, and 1037 $kg\ m^{-3}$) that roughly demarcate the boundaries between the AMOC's upper and lower limbs, and between the lower limb and the Nordic Seas overflow waters, respectively.

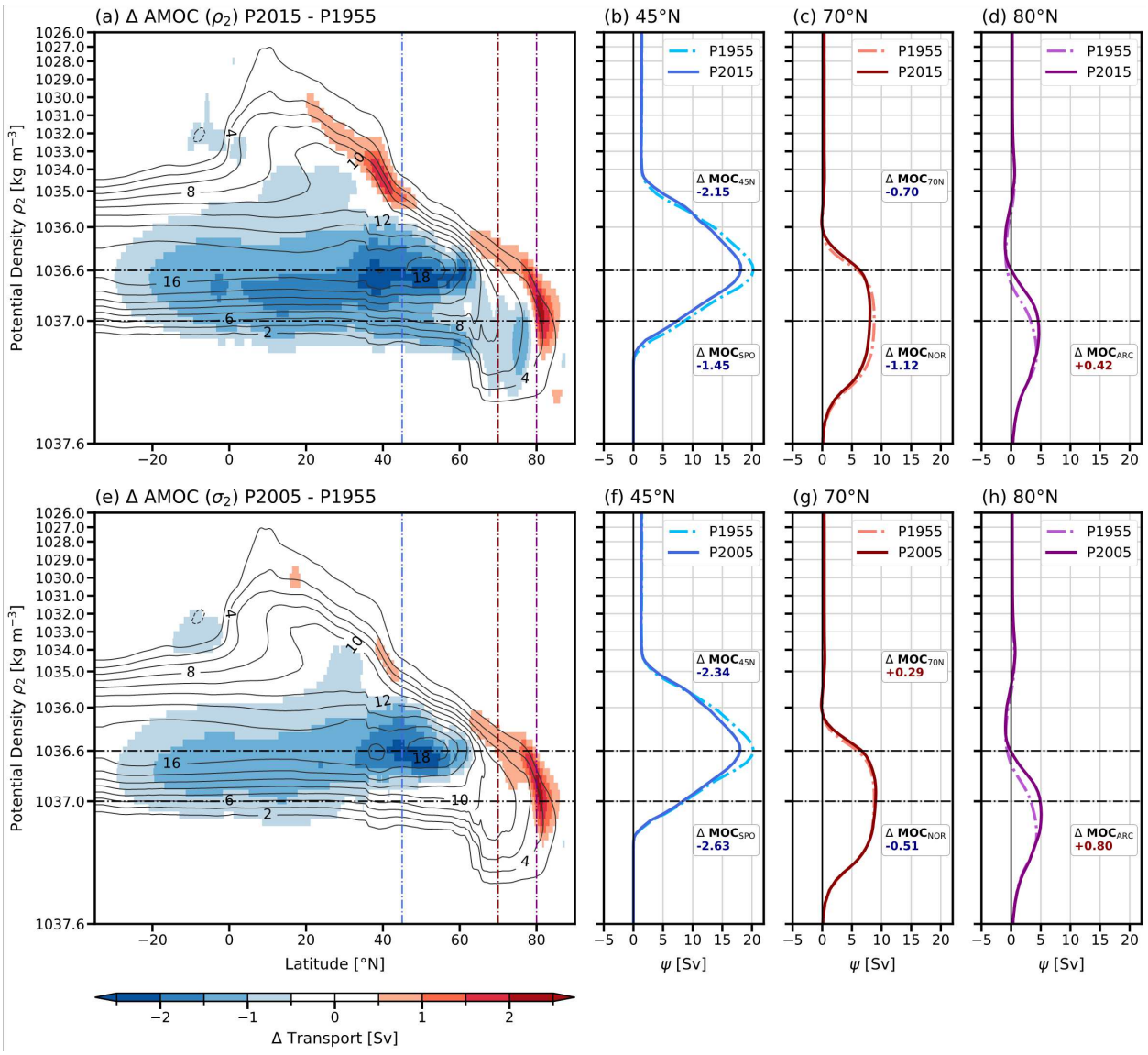
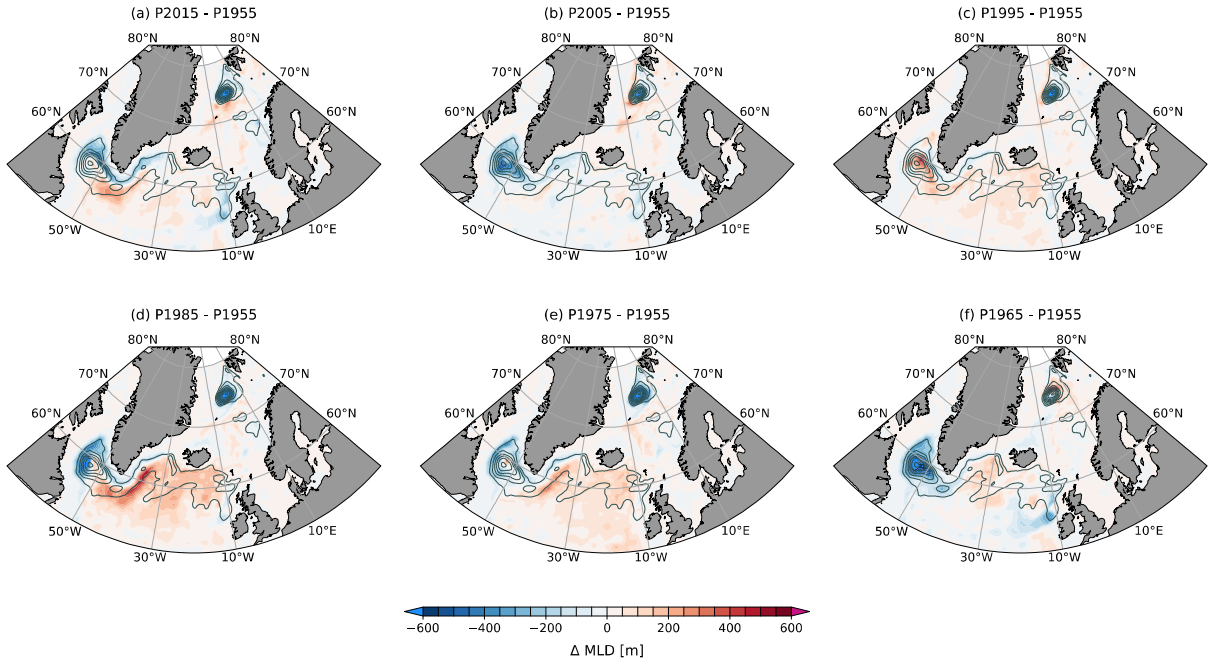


Figure 3. **AMOC streamfunction and profiles for the 2005–2014 and 2015–2022 decadal periods**. (a, e) Total AMOC streamfunction in potential density (ρ_2) coordinates against latitude for **a** 2025–2022, and **b** 2005–2014 periods. Contour lines represent the total transport, while color shading indicates the transport anomaly relative to the 1955–1964 baseline period. (b–d, f–h) Profiles of the AMOC in ρ_2 across 45°N, 70°N, and 80°N. Solid lines in (b–d, f–h) denote the specified decadal period, and dashed lines (b–d, f–h) represent the baseline period. Inset boxes indicate the transport difference (ΔMOC) for specific regional components. Analysis periods are

denoted by their initial boundary years (e.g., P1955 represents the 1955–1964 baseline, and P2015 represents 2015–2022). The vertical dash-dot lines in (a, e) indicate 45°N, 70°N, and 80°N latitudes, while the horizontal dash-dot lines in (a, e) indicate two ρ_2 isopycnal horizons (1036.6, and 1037 $kg\ m^{-3}$) that roughly demarcate the boundaries between the AMOC's upper and lower limbs, and between the lower limb and the Nordic Seas overflow waters, respectively.



62

63 **Figure 4**. **March Mixed Layer Depth (MLD) anomalies**. (a-f) Contour lines represent the total
64 March MLD for the 1955–1964 baseline period, while color shading indicates the difference in
65 March MLD between each of the six specified decadal periods (**a** 2015–2022, **b** 2005–2014, **c**
66 1995–2004, **d** 1985–1994, **e** 1975–1984, and **f** 1965–1974) and the 1955–1964 baseline period.
67 Blue shading indicates a shoaling of the mixed layer (suppressed convection), while red shading
68 indicates a deepening (enhanced convection). Analysis periods are denoted by their initial
69 boundary years (e.g., P1955 represents the 1955–1964 baseline, and P2015 represents 2015–
70 2022).

71

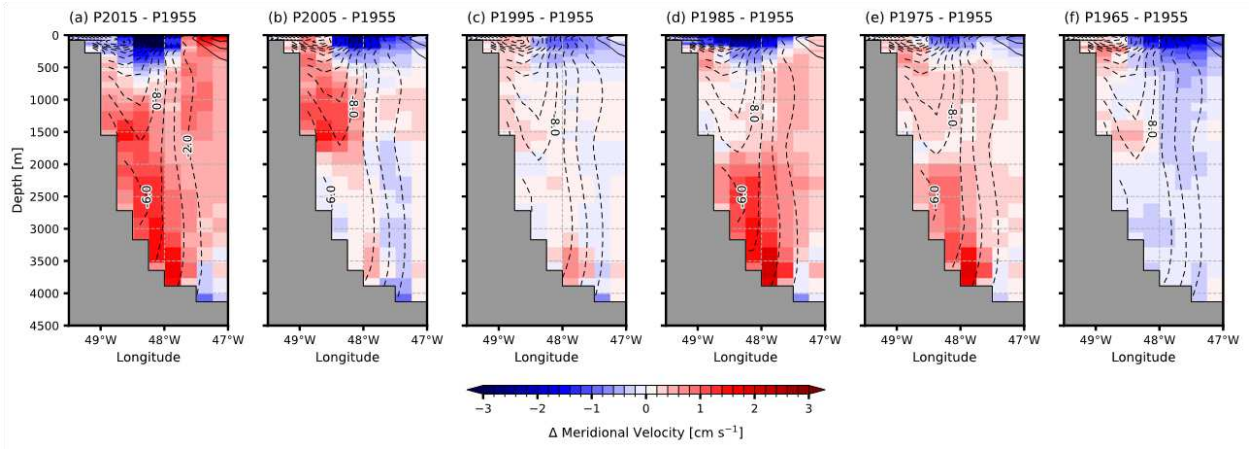
72

73

74

75

76



77

78 **Figure 5**. **Deep Western Boundary Current (DWBC) anomalies**. (a–f) Cross-sections across
79 45°N off the Grand Banks of Newfoundland (49.5°W to 47°W) showing anomalies in meridional
80 velocity for all six decadal periods (**a** 2015–2022, **b** 2005–2014, **c** 1995–2004, **d** 1985–1994, **e**
81 1975–1984, and **f** 1965–1974) relative to the 1955–1964 baseline period. Contours represent the
82 total southward velocity, and color shading represents the anomaly. Red shading indicates a
83 positive anomaly (a weakening of the southward flow), while blue shading indicates a negative
84 anomaly (an intensification of the southward flow). Analysis periods are denoted by their initial
85 boundary years (e.g., P1955 represents the 1955–1964 baseline, and P2015 represents 2015–
86 2022).

87

88

89

90

91

92

93

94

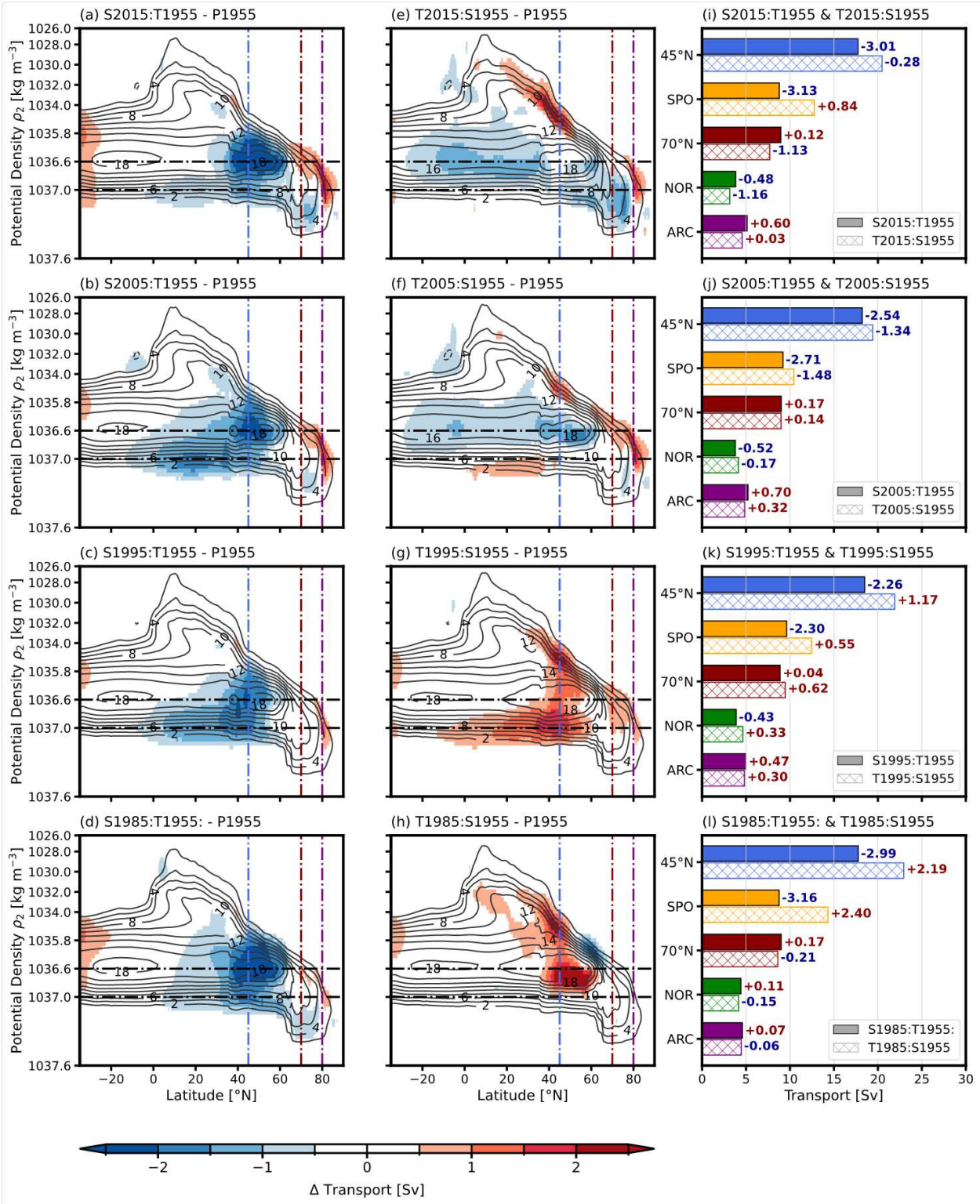
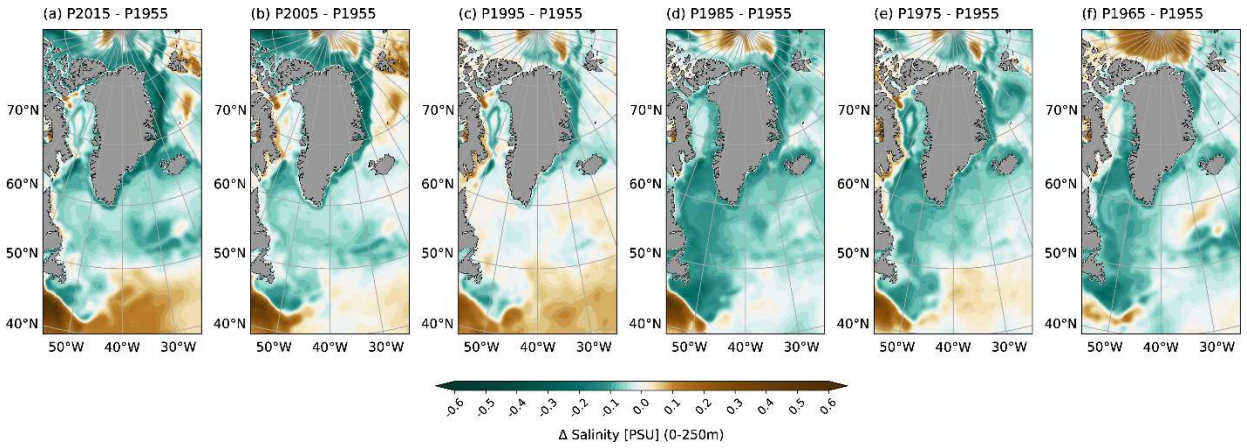


Figure 6. Attribution of AMOC changes to salinity and temperature forcing from the 1985–1994 to 2015–2022 periods. (Left Column) AMOC streamfunction anomalies for sensitivity

runs constrained by decadal salinity but relaxed to baseline temperature. (Middle Column) Anomalies for runs constrained by decadal temperature but relaxed to baseline salinity. (Right Column) Bar plots quantifying the isolated salinity and temperature effects on regional MOC components. S2015:T1955, for example, denotes the experiment constrained by 2015–2022 salinity and 1955–1964 temperature, whereas T2015:S1955 denotes the experiment constrained by 2015–2022 temperature and 1955–1964 salinity. P1955 denotes the 1955–1964 baseline period. The vertical dash-dot lines in (a–h) indicate 45°N, 70°N, and 80°N latitudes, while the horizontal dash-dot lines in (a–h) indicate two ρ_2 isopycnal horizons (1036.6, and 1037 $kg\ m^{-3}$) that roughly demarcate the boundaries between the AMOC's upper and lower limbs, and between the lower limb and the Nordic Seas overflow waters, respectively. See Figure S3 for S1975:T1955, S1965:T1955, T1975:S1955, and T1965:S1955.



121

122 **Figure 7**. **Upper-ocean (0–250 *m*) salinity anomalies from the Arctic to the Subpolar North**
123 **Atlantic**. Time-averaged salinity anomaly of the upper 250 *m* for each of the six decadal periods
124 (**a** 2015–2022, **b** 2005–2014, **c** 1995–2004, **d** 1985–1994, **e** 1975–1984, and **f** 1965–1974)
125 relative to the 1955–1964 baseline period. Analysis periods are denoted by their initial boundary
126 years (e.g., P1955 represents the 1955–1964 baseline, and P2015 represents 2015–2022).

127

128

129

130

131

132

133

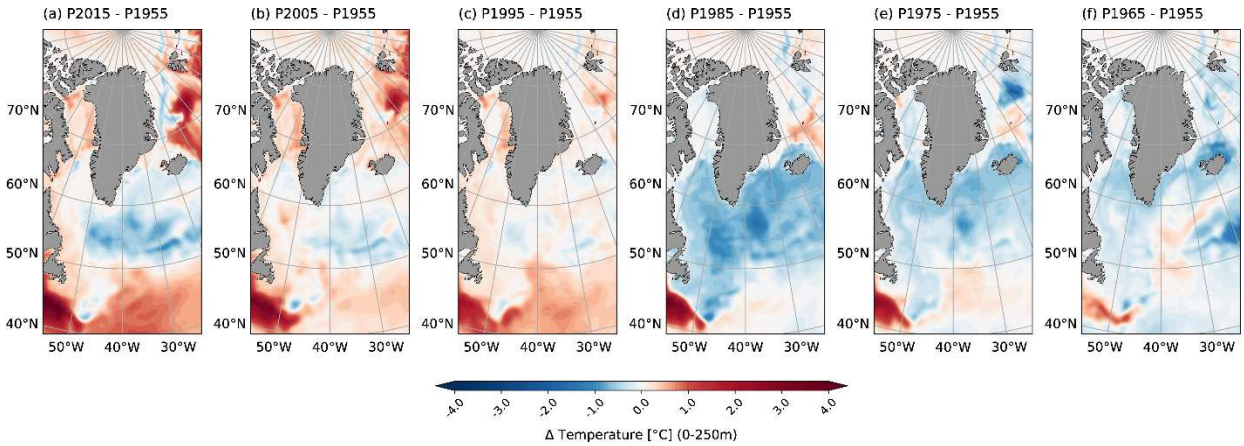
134

135

136

137

138



139

140 **Figure 8**. **Upper-ocean (0–250 *m*) temperature anomalies from the Arctic to the Subpolar**
141 **North Atlantic**. Time-averaged temperature anomaly of the upper 250 *m* for each of the six
142 decadal periods (**a** 2015–2022, **b** 2005–2014, **c** 1995–2004, **d** 1985–1994, **e** 1975–1984, and **f**
143 1965–1974) relative to the 1955–1964 baseline period. Analysis periods are denoted by their
144 initial boundary years (e.g., P1955 represents the 1955–1964 baseline, and P2015 represents
145 2015–2022).

Supplementary Files

This is a list of supplementary files associated with this preprint. Click to download.

- leeetalsupcommee.docx